# Implementation of biohybrid olfactory bulb on a high-density CMOS-chip to reveal large-scale spatiotemporal circuit information

Xin Hu [a], Shahrukh Khanzada [a], Diana Klütsch [a], Federico Calegari [b], Hayder Amin [a,*]

[a] *Biohybrid Neuroelectronics Laboratory, German Center for Neurodegenerative Diseases (DZNE), Dresden, Germany*
[b] *Proliferation and Differentiation of Neural Stem Cells, Center for Regenerative Therapies TU Dresden (CRTD), Dresden, Germany*

## ABSTRACT

Large-scale multi-site biosensors are essential to probe the olfactory bulb (OB) circuitry for understanding the spatiotemporal dynamics of simultaneous discharge patterns. Current ex-vivo biosensing techniques are limited to recording a small set of neurons and cannot provide an adequate resolution, which hinders revealing the fast dynamic underlying the information coding mechanisms in the OB circuit. Here, we demonstrate a novel biohybrid OB-CMOS biosensing platform to decipher the cross-scale dynamics of the OB electrogenesis and quantify the distinct neuronal coding properties. The approach with 4096-microelectrodes offers a non-invasive, label-free, bioelectrical imaging to decode simultaneous firing patterns from thousands of connected neuronal ensembles in acute OB slices. The platform can measure spontaneous and drug-induced extracellular field potential activity with substantially improved spatiotemporal resolution over conventional OB-based biosensors. Also, we employ our OB-CMOS recordings to perform multidimensional analysis to instantiate specific neurophysiological metrics underlying the olfactory spatiotemporal coding that emerged from the OB interconnected layers. Our results delineate the computational implications of large-scale activity patterns in functional olfactory processing. The systematic interplay of the experimental CMOS-base platform architecture and the high-content characterization of the olfactory circuit with various computational analyses endow significant functional interrogations of the OB information processing, high-spatiotemporal connectivity mapping, and global circuit dynamics. Thus, our study can inspire the design of advanced biomimetic olfactory-based biosensors and neuromorphic approaches for diagnostic biomarkers and drug discovery applications.

## 1. Introduction

The olfactory bulb (OB) is a vital chemosensory structure of the information coding mechanisms (Mori et al., 1999). It allows vertebrates to process and discriminate vast complex odorants and distinguish them with high selectivity and sensitivity (Buck and Axel, 1991; Bushdid et al., 2014). The OB's neuronal processes are distributed intricately, composed of an abundance of dendrodendritic interactions and a stratified structure in five connected layers (Price and Powell, 1970; Price and Powell, 1970). The OB also renders a distinctive form of morpho-functional neuronal plasticity conferred by a constant supply of new neurons (i.e., adult neurogenesis), allowing profound remodeling of the bulbar circuit in response to experience and challenges (Lepousez et al., 2013).

This organization represents a high degree of plasticity and the first relay station of olfactory perception with downstream information processing from the primary sensory epithelium to high-order neurons in subcortical and cortical areas for odor identification and interpretation (Doucette et al., 2011; Shepherd, 1972; Lledo et al., 2005).

This high dimensionality of olfactory processing and odor coding properties inspired the development of biomimetic olfactory sensors, i. e., electronic noses (Wilkens and Hartman, 1964; Persaud and Dodd, 1982; Ikegami and Kaneyasu, 1985). They promise potential advances in medical diagnosis, food quality, environmental, and military applications (Diclehan et al., 2019). However, a fundamental inherent shortfall in these electronic nose systems is the lack of realistic dynamics at the physiological cellular and network levels, thus hindering this technology's exploitation for further challenging applications (Göpel, 1998). Hence, considerable achievements in genetic, biotechnology, and bioengineering have been put forth to enable the implementation of olfactory cell-based biosensors (i.e., bioelectronic noses) (Göpel, 1998, 2000) to circumvent the limitations of conventional electronic noses and

to promote specific measurement of target odorants (Dung et al., 2018). In this context, many studies have been reported to employ a range of different olfactory cell-based biosensors (Dung et al., 2018; Liu, 2015; Wasilewski et al., 2017). Notably, a roadmap for advancing this technology has focused on deciphering the inherent plasticity mechanisms of olfactory information encoded in the orchestrated spatiotemporal activity patterns to refine and stabilize the OB sensory information (Lledo et al., 2005). These patterns are rhythmic neuronal synchronizations that encompass time-varying spatial distributions of discrete spike trains superimposed and complemented with a slow oscillation $<\sim 300$ Hz of the local field potentials (LFPs) that reflect subthreshold integrative processes (Panzeri et al., 2014; Buzsáki et al., 2012; Gelperin and Tank, 1990).

On the other hand, the mammalian olfactory system generates rhythmic oscillations of LFPs that exhibit a functional role in local odor processing and odor discrimination (i.e., gamma frequency band; 40–100 Hz) (Rojas-Líbano and Kay, 2008), odor learning and experience (i.e., beta band; 15–30 Hz) (Kay, 2014), and respiratory oscillations overlapping with the (theta band; 2–12 Hz) (Kay, 2005). Thus, investigating the electrophysiological properties is crucial to further understanding the local OB functional circuit connections and behavior and shaping sensory processing. In view of these demands, many previous studies have used cell or slice-based biosensors to report experimental paradigms and classical recording techniques for different olfactory signal biosensing such as microelectrode arrays (MEAs) (TIAN et al., 2017; Zhuang et al., 2021; Micholt et al., 2013), semiconductor field-effect transistors (Schöning et al., 2000; Kwon et al., 2015), patch-clamp recordings (Gelperin et al., 1993), light addressable potentiometric sensors (Liu et al., 2006), quartz crystal microbalance (Ko and Park, 2005), electrochemical impedance spectroscopy (Alfinito et al., 2010), and surface Plasmon resonance (Lee et al., 2006).

Also, these efforts are aided by insights from computational models (Linster and Cleland, 2001) and neuromorphic computing (Imam and Cleland, 2019). Despite MEAs shortcomings (i.e., low spatial resolution due to low numbers of recording electrodes), this method enables non-invasive, multi-site, long-term, and label-free probing of neuronal firing activity without disruption of cellular integrity. Recently, the manufacturing of low-cost semiconductor techniques based on complementary metal-oxide-semiconductor (CMOS) technology has been introduced into the design of biosensors (Ingebrandt, 2015) and the implementation of a high-density active-pixel sensor (APS) MEAs (Berdondini et al., 2005; Imfeld et al., 2008). Thereafter, APS CMOS-MEAs have been exploited in a wide range of neuroscience and bioengineering applications (Amin et al., 2016, 2017a, 2017b). Their unique inherent features with on-chip addressing and multiplexing and high signal-to-noise ratio (SNR) allow the measurement of neural signals at high spatiotemporal resolution with simultaneous recordings from several thousands of electrodes both in vitro (Berdondini et al., 2005; Imfeld et al., 2008) and in vivo (Angotzi et al., 2019). In turn, these features enabled large-scale recordings and network information analysis from the interaction of various neuronal components to facilitate understanding of the mechanisms that give rise to behavior-dependent cell assembly patterns (Buzsáki, 2004). However, spatiotemporal circuit interactions underlying OB coding mechanisms have remained mostly elusive, hindering the development of advanced olfactory-cell-based sensors. Although existing olfactory-MEA biosensors have endowed valuable results, a clear understanding of the interareal coordination of bulbar circuitry mechanisms has lagged behind.

In this study, we report a novel Biohybrid Olfactory Neural Circuit on a CMOS-chip (BIONICS) capable of recording massively simultaneous neuronal firing patterns in acute mouse OB slices. The platform integrates large and dense electrode arrays (i.e., 4096-microelectrodes) and on-chip signal processing implemented in a CMOS-chip. The combination of the OB circuit and the high-density electrode configuration allows recording real-time spontaneous and pharmacologically-evoked activation of the OB neural circuit from thousands of connected neuronal ensembles within the interareal layers of the OB operated in ex vivo. We further exploit our OB-CMOS-chip recordings with fundamental basic and advanced analyses to instantiate specific neurophysiological metrics underlying the olfactory spatiotemporal information that emerged from the OB interconnected layers. Therefore, we characterize the rhythmic oscillations of the LFPs, oscillatory frequency bands, and coherence magnitude for single electrode activity as well as between OB layers. We also identify the event initiation onsets and quantify the dynamic profiles of signal propagation patterns. The rich information ingrained in our unique datasets also allows us to compute the spatial neural sources that contribute to the LFPs by using the kernel current source density (kCSD) method, functional connectivity (FC) maps, and topological interaction of thousands of active OB neuronal ensembles that delineate the construction of functional OB circuitry. Finally, we validated our platform to unveil a large-scale functional remodeling in the OB circuitry due to ongoing neurogenesis using a well-established and reported mouse model of enhanced neural stem cell expansion (Bragado Alonso et al., 2019; Artegiani et al., 2011; Berdugo-Vega et al., 2020).

To our knowledge, this is the first report of a high-density CMOS-neurochip that allows revealing the spatiotemporal functional processing in the interconnected OB circuit. Deciphering the mechanism of large-scale OB electrogenesis will enhance our understanding of the neuronal ensembles' functional organization. It will also provide an effective tool to investigate information processing and spatiotemporal coding in the OB circuit. Together, our results offer vital evidence for the future development of biomimetic olfaction detection biosensors for various applications.

## 2. Materials and methods

**Animals and OB acute slices preparation.** All experiments were performed on 8 weeks C57BL/6j (Charles River Laboratories, Germany) and triple transgenic 4D- and 4D+ mice, previously described (Bragado Alonso et al., 2019). All work and animal procedures were performed in accordance with the applicable European and national regulations (Tierschutzgesetz) and were approved by the local authority (Landesdirektion Sachsen; 25–5131/476/14 and DD24-9168.11-1/2011-11, TVV13/2016, and HD35–9185.81/G-61/15). Mice were anesthetized with isoflurane before decapitation. The brain and OB were carefully removed from the skull and placed in a chilled cutting sucrose solution before slicing. The Brain and OB were fixed on the cutting plate, and horizontal slices (300 μm thick) were prepared using Leica Vibratome VT1200S (Leica Microsystems, Germany). Slices were cut at 0–2 °C in aCSF solution saturated with 95% $O_2$ and 5% $CO_2$ (pH = 7.2–7.4) of a high sucrose solution containing in mM: 250 Sucrose, 10 Glucose, 1.25 $NaH_2PO_4$, 24 $NaHCO_3$, 2.5 KCl, 0.5 Ascorbic acid, 4 $MgCl_2$, 1.2 $MgSO_4$, 0.5 $CaCl_2$. Next, OB slices were incubated for 45 min at 34 °C and then allowed to recover for at least 1 hour at room temperature before used for recordings with CMOS-chips, in a recording aCSF solution containing in mM: 127 NaCl, 2.5 KCl, 1.25 $NaH_2PO_4$, 24 $NaHCO_3$, 25 Glucose, 1.2 $MgSO_4$, 2.5 $CaCl_2$, and the solution was aerated with 95% $O_2$ and 5% $CO_2$.

**Biohybrid OB-CMOS biosensor recordings.** We performed all extracellular recordings using CMOS-biosensors and an acquisition system (3Brain AG, Switzerland) customized to our BIONICS setup. CMOS chips integrate 4096 recording electrodes with a 42 μm pitch size to compose an active sensing area of $\sim 7$ mm$^2$, ideal for recording from the entire $\sim 4$ mm$^2$ OB tissue. The on-chip amplification circuit allows for 0.1–5 kHz band-pass filtering conferred by a global gain of 60 dB sufficient to record slow and fast oscillations. Modular Stereo microscope Leica MZ10F (Leica Microsystems, Germany) was designed and incorporated into the setup to capture OB slices' light-imaging simultaneously with the whole-circuit firing pattern recordings. All CMOS chips were coated with 0.1 mg/ml PDLO (Sigma-Aldrich, Germany) and

incubated for 30 min at 37 °C before recordings. Then, slices were moved onto chips, and the coupling between OB slices and CMOS-electrodes was enhanced with a custom-made platinum harp placed above the tissue. Slices were perfused continuously with an oxygenated recording solution at 4 ml/min. We collected 10 min of spontaneous and pharmacological-induced extracellular recordings at 14 kHz/electrode sampling frequency and stored them for offline analysis. We used Brain wave software (3Brain AG, Switzerland) for data recording and employed a hard threshold algorithm to perform LFP detection with a 10 ms refractory period and a 500 ms maximum event duration.

**Drug treatment.** We prepared fresh solutions of all drugs for each experiment by dissolving the drug in the recording solution. The final working concentrations used for all experiments were 100 μM, 30 μM, and 10 μM of 4-aminopyridine (4AP), Bicuculline (BiC), and dizocilpine (MK-801) (Sigma-Aldrich, Germany), respectively.

**Immunohistochemistry and fluorescence imaging.** Brains with OB were perfused and post-fixed overnight in 4% PFA at 4 °C. Immunohistochemistry was performed as described (Bragado Alonso et al., 2019). The images were acquired with an automated Zeiss ApoTome confocal microscope (LSM 780, Carl Zeiss, Germany).

**Data Analysis.** All basic and advanced algorithms used in this study were developed as custom-written Python scripts.

**Mean activity basic analysis.** We selected four parameters to describe the mean activity features of large-scale spatiotemporal LFP oscillations, including amplitude, energy, frequency, and duration. The signal amplitude analysis was obtained by full-wave rectification and low-pass filtering (cutoff frequency 100 Hz). The energy is defined as the area under the squared magnitude of the LFP rates for a specific time window.

**Lognormal distribution.** The LFP firing patterns of the OB neuronal ensembles showed a wide degree of participation in the circuit activity and followed a skewed lognormal distribution. Thus, we computed the probability density function for the lognormal distribution:

$$p(x) = \frac{1}{x\sigma\sqrt{2\pi}}e^{-(lnx-\mu)^2/2\sigma^2}$$

Where $\mu$ is the mean, and $\sigma$ is the standard deviation.

**Gini coefficient and CV$_2$.** To quantify the inequality of participation of individual neurons in the OB circuit, we employed the Gini index as a commonly used measure of inequality and sparsity (Hurley and Rickard, 2009) and computed as the ratio of the areas on the Lorenz curve diagram:

$$Gini = \frac{A}{A+B}$$

Where $A$ is the area above the Lorenz curve, and $B$ is the area below for the cumulative LFP firing rates.

To assess the local-trial variability of the firing patterns, we used the coefficient of variation (CV$_2$) (Holt et al., 1996), which is defined as the function of pairs of adjacent inter-LFP-event intervals $IEI_i$ and $IEI_{i+1}$ divided by the average of the event intervals.

$$CV_2(i) = \frac{2|IEI_i - IEI_{i+1}|}{IEI_i + IEI_{i+1}}$$

**Time-frequency and PSD analyses.** We first constructed the frequency-time dynamics in pseudo-color spectrograms for a selected 10 s time window using filtered LFPs (1–100 Hz). Next, we computed the Periodograms to identify dominant frequencies in the oscillatory activity in a given time-series. The spectra were calculated using Welch's method (Welch, 1967) by calculating the Fast Fourier Transform of the recorded LFPs to estimate the power spectral density (PSD).

**Waveform classification.** To characterize and allocate the non-sinusoidal shapes of the recorded LFP waveforms to their OB layers, we developed a procedure consisting of four steps. First, (waveform extraction) - we detected active firing electrodes clustered based on their structural relation to the OB layers. We extracted information from hundreds of waveform segments that occurred at least in three consecutive LFP events. Second, (Pre-processing) – all detected and extracted waveforms were denoised by hard threshold algorithm and filtered by Low-pass filter (1–100 Hz). Third, (Parameter Identification) – we defined in our extracted waveforms four features, including amplitude (waveform height feature), period, rise-decay symmetry (slope features), and area (area feature). Fourth, (classification and clustering), we reduced the dimensionality of the computed waveform features using the Principal Component Analysis (PCA) and K-means clustering algorithms (Ding and He, 2004) to identify best-classified waveform shapes into five clusters associated with the GL, GCL, PL, ONL, and OCx layers. To evaluate the accuracy of the cross-layer classification, we computed the average true positive value across-layer classes represented as the mean diagonal probability of the confusion matrix. The diagonal probability represents the results of the predicted labels when matching the actual class labels computed as the sum of the diagonal elements divided by the number of class samples, and it is between (0, 1).

**Spatiotemporal coherence.** To measure the predictable relationship between firing LFP rates at different spatial locations of the OB circuit, we calculated the 2D spatial coherence maps. We calculated the correlation between pairs of firing electrodes of the CMOS-chip (64 x 64 electrodes) arranged in rows (x) and columns (y). The function is a dimensionless quantity and ranges between (0, 1) and is defined as (Cooper Roddey et al., 2000):

$$C_{xy}(f) = \frac{|P_{xy}(f)|^2}{P_{xx}(f)P_{yy}(f)}$$

Where $P_{xx}(f)$ and $P_{yy}(f)$ are the autospectral density of the firing x and y, respectively, and $P_{xy}(f)$ is the cross-spectrum density of the firing x and y estimated using Welch's method. A Spatial coherence near one indicates that the active electrodes encode all information of the firing rate of that spectral frequency component. In contrast, a value close to zero indicates no information of the firing is present.

Further, to quantify the temporal spectral coherence with the cross-frequency synchrony (i.e., coherence as a function of frequency across event time) in cross-OB layers, the pairwise coherence magnitudes in the frequency domain of cross-layers were considered between each active electrode in the reference layer and all other active electrodes from paired layers. Then, we computed the average coherence across frequencies of paired layers in the OB circuit and compared them in different drug treatments. Higher coherence values (near 1) render the similarity of signal phases and phase-locked at a specific frequency, whereas lower coherence values refer to dispersed signal phases.

**LFP propagation dynamics.** To quantify the propagation magnitude of the spatiotemporal LFP Events in all interconnected OB layers, we employed the center-of-activity trajectories (CATs) analysis (Gandolfo et al., 2010; Chao et al., 2007). We used the voltage values embedded in the LFP frame activities within 5 ms moving time bins to collect the CAT magnitudes in each firing event. The value of the CA at time $t$ is a two-dimensional vector defined as:

$$\overrightarrow{CA}\,(t) = [CA_x,\ CA_y] = \frac{\sum_{E=1}^{n} V_{tm}(E) \cdot [Col(E) - R_{col}, Row(E) - R_{row}]}{\sum_{E=1}^{n} V_{tm}(E)}$$

Where $V_{tm}(E)$ represents the LFP firing rate corresponding to the active electrodes $E$ within a time window *(tm)*. Also, $Col(E)$ and $Row(E)$ are the column and row numbers of the associated $E$. Then, $R_{col}$ and $R_{row}$ are the coordinates of the physical center of 64 x 64 electrodes. $n$ is the total number of active electrodes. Then, the CA trajectory from $t_0$ to $t_1$ with a time step $\Delta t$ is defined as:

$$\overrightarrow{CAT}\,(t_0, t_1) = \overrightarrow{CA}\,(t_0),\ \overrightarrow{CA}\,(t_0 + \Delta t),\ \overrightarrow{CA}\,(t_0 + 2\Delta t),\ ....,\ \overrightarrow{CA}\,(t_1)$$

**Velocity of conduction.** To track the putative displacement of $\overrightarrow{CA}$ LFP events in the entire interconnected OB circuit, the velocity of conduction was calculated as the average of instantaneous vector quantity displacements calculated for the time of a propagating LFP event and expressed as:

$$\overrightarrow{Velocity} = \frac{\overrightarrow{\Delta d}}{\Delta t}$$

Where $\Delta d$ is the change in displacement and $\Delta t$ is the change in time.

**Functional connectivity and causal links.** To infer the large-scale statistical dependent connectivity in a multilayered OB network, we first calculated the cross-covariance between pairs of active electrodes in the 64 x 64 array using the Pearson correlation coefficient (PCC) (Eggermont et al., 2011). The correlation coefficient between electrodes was then sorted based on the OB layers and presented in a symmetric matrix. The PCC is defined as:

$$PCC_{xy} = \frac{n \sum xy - \sum x \sum y}{\sqrt{n \sum x^2 - (\sum x)^2} \sqrt{n \sum y^2 - (\sum y)^2}}$$

Where $x, y$ denoted the values of pair electrodes time series for $n$ number of the active array.

Then, we performed the Multivariate Granger causality by fitting a vector autoregressive model to the time series to quantify the influence of one time series on another (Damos, 2016). To measure the directional information flow within the correlated links in the network, we performed the Directed Transfer Function (DTF) (Kaminski and Blinowska, 1991).

**Current source density.** To estimate the current sources generating the extracellular low-frequency potentials recorded in all OB layers, we used the Kernel Current Source Density (kCSD) Analysis (Potworowski et al., 2012), described in the kCSD-python package and available on GitHub (https://github.com/Neuroinflab/kCSD-python).

**Network efficiency and wiring cost.** To quantitatively measure a precise information flow and exchange of parallel integrated processing in the interconnected OB network, we used the measure of global, local efficiencies (Latora and Marchiori, 2001), and connection cost. These are dimensionless measures ranging from 0 to 1. The global efficiency can be defined as the inverse of the average of shortest path lengths between all nodes in the network and calculated as:

$$E_{global} = \frac{1}{N(N-1)} \sum_{i \neq j \in G} \frac{1}{L_{i,j}}$$

Where $N$ is the number of all nodes in the network, $L_{i,j}$ is the average path length between all nodes in the network.

Further, based on local clusters, the local efficiency is the average efficiency of clusters (subgraph) for a node with the neighbors, and calculated as:

$$E_{local} = \frac{1}{N_{G_i}(N_{G_i} - 1)} \sum_{k \neq j \in G_i} \frac{1}{L_{k,j}}$$

Where $N_{G_i}$ is the number of nodes in the local subgraphs (clusters) $G_i$ of the network, $L_{k,j}$ is the path length between pair nodes in the cluster.

**Wiring cost.** The network cost was estimated based on the minimum spanning tree (MST) method using the Kruskal algorithm. This approach calculates the shortest path length connecting all network nodes at the cheapest cost.

**Statistical analysis.** All statistical analyses were performed with Originlab 2020. All data in this work were expressed as the mean ± standard error of the mean (SEM). All box charts are determined by the 25th- 75th percentiles, and the whiskers by the 5th- 95th percentiles, and lengths within the Interquartile range (1.5 IQR). Also, the lines depict the median and the squares for the mean values. Differences between groups were examined for statistical significance, where appropriate, using one-way analysis of variance (ANOVA) or two-way ANOVA followed by Tukey's posthoc testing. $P < 0.05$ was considered significant.

## 3. Results and discussion

In what follows, we first developed and implemented a hybrid biosensor platform by integrating the OB circuit into a CMOS-MEA chip, which allowed us to record LFPs and spikes from the OB multi-layers. Next, we exploited the multidimensional data focusing on the LFPs to infer and provide new insights about the subthreshold integrative processes in high spatiotemporal resolution expressed by extracting unique dynamic features of the oscillatory activity and functional mapping across the OB circuitry. (i.e., frequency spectrum, coherence, cross-correlation, causal connectivity, and assessing neurogenic remodeling effect).

### 3.1. Implementation of the large-scale BIONICS platform

To quantitatively probe the large-scale firing patterns and characterize the olfactory spatiotemporal coding of the whole-multilayered OB, we engineered a biohybrid OB-CMOS biosensor platform (BI-ONICS) (Fig. 1). It combines isolated whole-OB acute slices and a CMOS-chip. The OB-CMOS-chip was continuously perfused with an optimized aCSF to maintain high viability and stable, functional responses for several hours (*n = 24 slices from 8 adult mice at 8 weeks old*). Also, we employed optical imaging into the bioelectrical OB-CMOS-based setup allowing the light-imaging acquisition of OB slices concurrently with the whole-circuit firing pattern recordings (Fig. 1a). The CMOS-chip integrates a 64 x 64 microelectrodes pixel array to allow the simultaneous recordings of sub-millisecond extracellular firing information from the entire OB circuitry (Fig. 1b). The active sensing area of the CMOS-chip is 2.69 x 2.69 mm (i.e., 4096 microelectrodes with a 42 μm pitch size) (Imfeld et al., 2008), which is compatible with the area of a whole mouse OB slice (i.e., 2 x 2 mm). Our OB-CMOS biosensor readout captured the real-time circuitry acquisition rendered by a single electrode (i.e., pixel-like) sensor from sequential bioimaging frames encoding olfactory functional information at high spatiotemporal resolution. The voltage values of each sensing pixel were mapped on large-scale OB layers with a pseudo-color scaling. The final construction illustrated real-time bioimaging video frames of the entire OB functional circuit (Fig. 1b, and Supplementary Movie 1). The CMOS-chip surface was functionalized
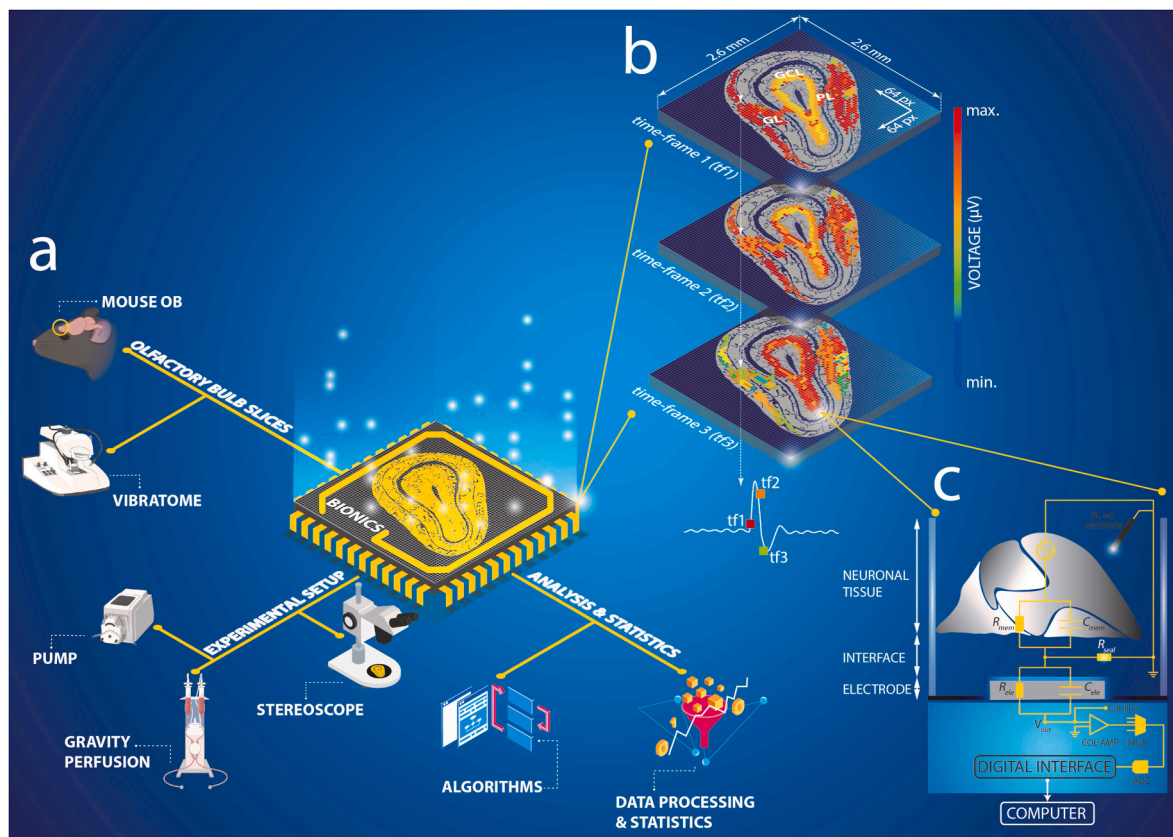
**Fig. 1. BIONICS setup and implementation. a)** Graphical isometric imaging setup featuring the biohybrid OB-CMOS-chip with 64x64 electrode array and integrating the experimental and analysis components. **b)** Pixel-multi-frame real-time representation of the encoded OB network-wide activity enabling pseudo-color reconstruction of the firing information from the sequential obtained frames. **c)** Cell model of tissue-electrode CMOS interface showing the pixel circuit configuration, the individual functional elements, and the communication interfaces. Surface functionalization with PDLO enhanced the slice-electrode coupling interface and increased the SNR (i.e., increased the $R_{seal}$). (For interpretation of the references to color in this figure legend, the reader is referred to the Web version of this article.)

using a specific adhesion-promoting molecule – poly-DL-ornithine (PDLO) (Amin et al., 2018) that enhanced the cell-electrode interface coupling and improved SNR by increasing the seal resistance ($R_{seal}$) between the tissue and the electrode (Fig. 1c).

Supplementary video related to this article can be found at htt ps://doi.org/10.1016/j.bios.2021.113834

*3.2. Features of spatiotemporal LFP firing patterns and activity-dependent distributions in multilayered OB circuits*

The neuronal processes in the OB instantiate in five connected layers, i.e., olfactory nerve layer (ONL), glomerular layer (GL), external plexiform layer (EPL), mitral cell layer (MCL), and granule cell layer (GCL) (Price and Powell, 1970; Price and Powell, 1970). In our study, we consider the EPL and the MCL as the projection layer (PL). In a canonical biological olfactory circuit, the olfactory sensory neurons (OSNs) project and converge their axons into the same glomeruli in the GL. Glomeruli represent the inhibitory functional units for information coding that shape the features of odorant responses (Imai, 2014). OSNs form excitatory synapses with mitral cells in the projection layer that, in turn, project their axons to the olfactory cortex (OCx) (Mombaerts, 2001).

To address the overarching benefit of the OB-CMOS-biosensor to

reveal different neuronal processes by their intrinsically generated firing patterns or the facilitation of synaptic transmission, we recorded the spontaneous and pharmacologically-induced large-scale responses in OB circuitry. We used three biochemical benchmark compounds including, 4-aminopyridine (4-AP) - potassium channel blocker, Bicuculline (BiC) - $GABA_A$ antagonist, and dizocilpine (MK-801) - N-Methyl-D-aspartate (NMDA) receptor antagonist. We computed several first-order statistical parameters (LFP energy, oscillation frequency, amplitude, and duration). Spontaneous oscillation and spiking activity were detected in all OB layers except the ONL. We found substantial responses of the OB circuit assessed by the statistical parameters shown in (Fig. 2a, *right*). We also illustrated the spatial organization of those large-scale metrics by overlaying the computed mean of the functional, statistical metrics obtained from the LFP recordings on the OB circuits' optical images (Fig. 2a *left*).

The collective functional representations given in firing patterns of synchronized neuronal populations have been shown to exhibit a skewed distribution of firing rates in other experimental setups (Amin et al., 2017a; Mizuseki and Buzsáki, 2013). Our large-scale OB recordings found similar highly skewed lognormal-like distributions of firing LFPs in GCL, Pl, and OCx layers (Fig. 2b). Those skewed distributions showed a range of low and high firing patterns indicating a
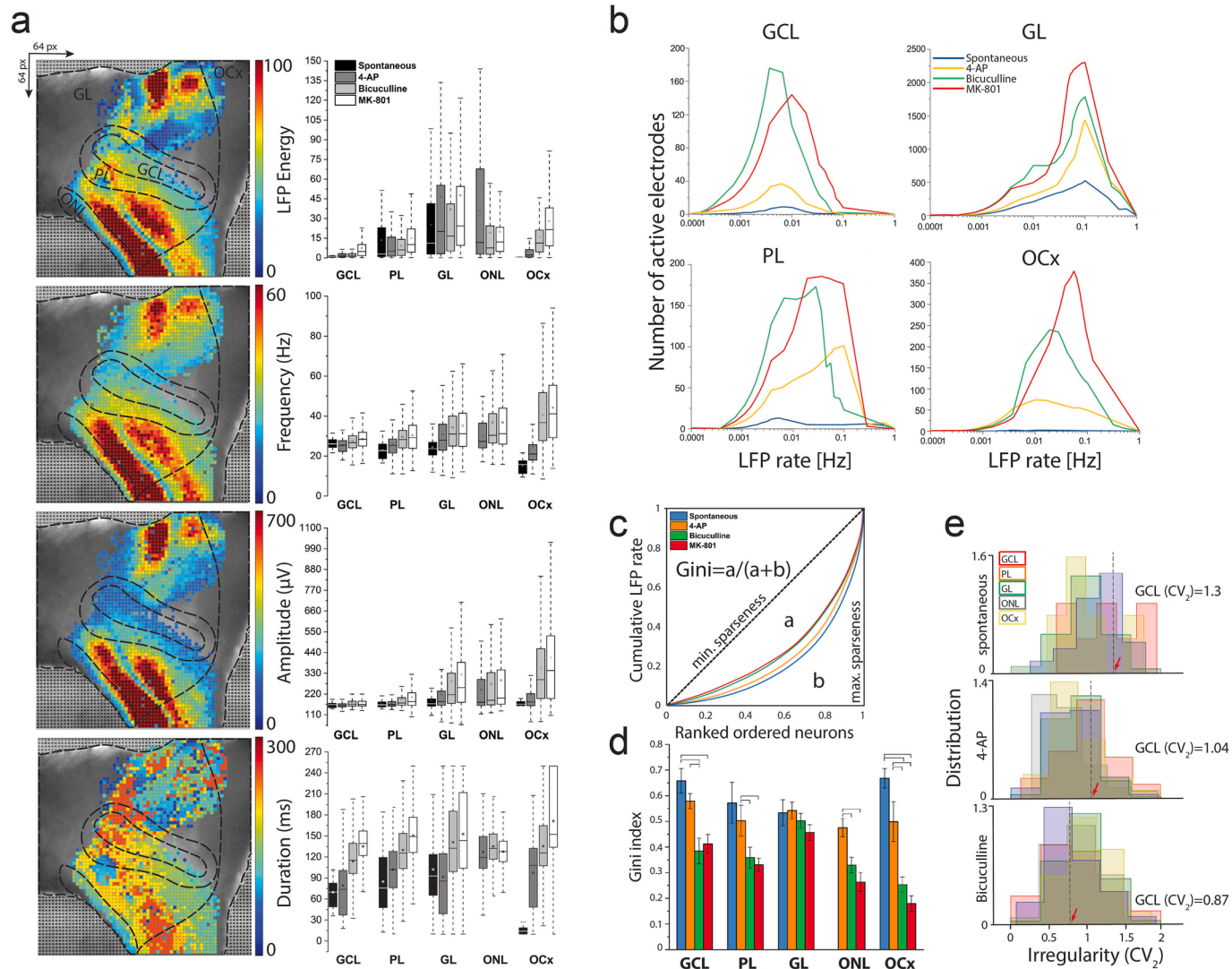
**Fig. 2. OB network-wide extracellular activity parameters and distribution. a)** Topographical representations and statistical characteristics of the large-scale firing patterns recorded simultaneously from the entire OB slices (i.e., 4AP induced activity example). Pseudo-color values of the energy, frequency, amplitude, and LFP activity duration superimposed to the OB structural images. The area under the squared magnitude of the LFP rates (LFP energy) is significantly higher in GL than in other layers, and frequency denotes a similar frequency oscillation range in all layers. The amplitude is also significantly higher in GL and increased with drug treatment; in contrast, the LFP events' duration is decreased with consecutive drug treatments. **b)** LFP firing events display a lognormal-like distribution in interconnected OB layers allowing to elucidate the network dynamics. **c)** Lorenze curve and Gini coefficient analysis indicate the in equal neuronal participation and sparseness. **d)** Gini coefficient quantification for the firing activity in all OB layers (*$p < 0.05$, **$p < 0.01$, ANOVA). e) $CV_2$ values ($0 \rightarrow 2$) showing the quantification of the spread of IEIs for the entire firing events. The $CV_2$ is reduced (towards regular pattern) after blocking the GABAergic population with BiC as indicated by moving red arrows to the left side (**$p < 0.01$, ANOVA, $n = 24$ slices from 8 mice). (For interpretation of the references to color in this figure legend, the reader is referred to the Web version of this article.)

network-wide firing fluctuation and a diverse repertoire of participating neurons to the circuitry firing information. In other words, when the OB circuit activity was enhanced by unbalancing the inhibition or excitation drive (i.e., BiC and MK-801 treatments), the firing distribution showed lognormal-like distributions in the GCL, PL, and OCx, but symmetric distribution in the GL, indicating a mixture of circuit firing regimes of fluctuation-driven and mean-driven, respectively (Petersen and Berg, 2016). Remarkably, this mixture of activity regimes within interconnected OB layers suggests a significance featured spatiotemporal patterns in maintaining the sensitivity and stability balance of the OB circuitry.

To parametrically evaluate the spatial sparsity and diversity of participating neurons (i.e., the efficiency of neuronal representations) rendered by their firing potentials, we used Lorenz statistics to generate the Gini coefficient (Hurley and Rickard, 2009). The Gini index is between zero and one and reflects the inequality of participation of neurons given by their firing LFP values; it is higher in the unequal participation of neurons to the firing activity (Fig. 2c). The Gini index was higher in the spontaneous recorded LFPs in all OB layers (i.e., particularity in GCL, PL, and OCx), which decreased along with the treatment of the compound of 4-AP, BiC, and Mk-801, respectively (Fig. 2d). This indicated that neuronal selectivity and the sparseness of representation in a given spontaneous activity reflected the strong activation of a relatively small group of cells. This is the first evidence of the sloppiness in spontaneously active OB layers. A small but stable subnetwork of neurons is critical for global stability, allowing considerable plasticity in the remaining majority of cell population (Panas et al., 2015).

On the other hand, the evoked-activity groups (i.e., BiC and MK-801) showed sloppiness but not sparseness, which inferred stiff dimensions involving more complicated combinations of other parameters following the circuit modulation. Despite the overall stability we observed in the OB functional representations, changes in the LFP timings were found upon manipulating the balance of inhibition and excitation by pharmacological treatment. To evaluate these changes in all OB layers, we quantified the LFP timings irregularity using the coefficient of variation index ($CV_2$) (Holt et al., 1996)(see methods). We found a significant decrease in the $CV_2$ (i.e., GCL = 1.3, 1.04, and 0.87) in spontaneous, 4-AP, and BiC conditions, respectively (Fig. 2e). This decrease in $CV_2$ values indicates decreased variability, hence, increased LFP regularity upon compound treatment. Altogether, our results delineate detailed spatiotemporal functional implications of discharge patterns in distinct subnetworks of the OB layers opt for stability and spatial information coding. This could emerge from the intrinsic biophysical properties of the individual ensembles in these circuits and their distinct wiring, as reported in other brain states (Mizuseki and Buzsáki, 2013).

### 3.3. Characterization of oscillatory-dependent features of LFPs and waveform classification

Next, we sought to identify the functional significance in the frequency and time domains of the LFP oscillatory synchronized waves rendered by the interconnected OB layers. Thus, we employed band-pass filters on the recorded data to set for high-frequency oscillation (HFO), indicating spiking activity and low-frequency-oscillation (LFO), indicating three prominent oscillatory bands in different layers (i.e., theta, beta, and gamma) (Fig. 3a). We observed slow and fast oscillations in nearly all layers under spontaneous and pharmacologically-modulated activity (Fig. 3a, GL and GCL layers examples). Then, we computed the synchronous frequency-time domain dynamics of a selected

electrode within the 4096-microelectrode array in pseudo-color spectrograms. This spectrogram exhibited superposed sustained oscillatory events in the GL layer lasting for several seconds with coordinated frequency peaks in the theta-gamma band (Fig. 3b, *left*).

Similarly (Fig. 3b, *right*), shows the GCL layer's spectrogram, where single transient pulses of oscillatory events occurred with a frequency range between 4 and 60 Hz. Further, we employed the power spectral density (PSD) analysis to simultaneously quantify a specific oscillatory band's power magnitude in the interconnected OB layers recorded by a full-CMOS array from spontaneous and drug-induced activity phases (Fig. 3c, and Supplementary Fig. 1). Despite the noticeable fluctuations in the power magnitude upon pharmacological manipulation, we found a prevailing network frequency oscillation in the theta band in all OB layers, predominantly in GCL and GL. These results confirm evidence on the rhythmic theta oscillations coordinated by the glomerular network (Fukunaga et al., 2014). Further, the theta-gamma coupled oscillations were also reported to emerge from the individual mitral cells (Margrie and Schaefer, 2003) and also found in hippocampal networks (Buzsáki and Draguhn, 2004). Our results suggest rhythmogenic subregions of the OB circuitry to drive distinct functional microcircuits that are vital for OB coding.

In addition, investigating the features of oscillatory waveforms and their shapes can better elucidate the contribution of individual neuronal populations in the spatially connected layers and the olfactory information coding (Schaworonkow and Nikulin, 2019). Therefore, we employed unsupervised classification analysis of LFP oscillations applied on hundreds of waveforms in each OB layer made possible by the multidimensional high spatiotemporal resolution CMOS-recordings. The analysis reliably yielded five well-separated waveform classes that indicated distinct firing pattern features in each OB layer (Fig. 3d, and e). The classification process was performed by PCA and clustering with the k-means algorithm (see methods). The separation of the classified clusters was quantified by computing the true probability of waveform classes in their layers based on the K-means underlying the clustering (Fig. 3f). The average accuracy of the classification process across all five classes was 92%, inferring well-defined featured clusters. This result supports the notion of waveform shapes of neural oscillations as stable physiological information inferring a layer-class marker in the OB circuitry with relevant functional roles to be further investigated.

Next, to identify the spatiotemporal oscillatory processes by the nonsinusoidal waveforms that we classified in the interconnected OB layers, we applied filters on the waveforms to quantify distinct temporal features of the spatially located OB layers (i.e., rise peak, decay peak) in three separate frequency oscillatory bands (i.e., theta, beta, and gamma) under different pharmacological-evoked conditions (Supplementary Fig. 2). We found a cross-frequency coupling in the oscillatory generators underlying each OB layer (GL, PL, and GCL), and their waveform shapes identified prominent theta rhythms. The waveform rise and decay peaks were significantly higher in the theta band under BiC and MK-801 administration in all layers compared to beta and gamma oscillatory bands. These results delineate the contribution of the waveform shapes in determining the oscillatory process generators in the OB network, mediated by the activation of NMDA receptors and the $GABA_A$ release (Schoppa, 1998), which play a role in generating theta rhythm, and modulating the OB spatiotemporal coding.

In sum, these results demonstrate an interplay between waveform shape features (temporal) and distinct OB layer characteristics (spatial) that could only be revealed by the simultaneous multi-site recordings at high SNR, which maintained the distinct physiological information and firing synchrony of those waveform shapes with specific-frequency
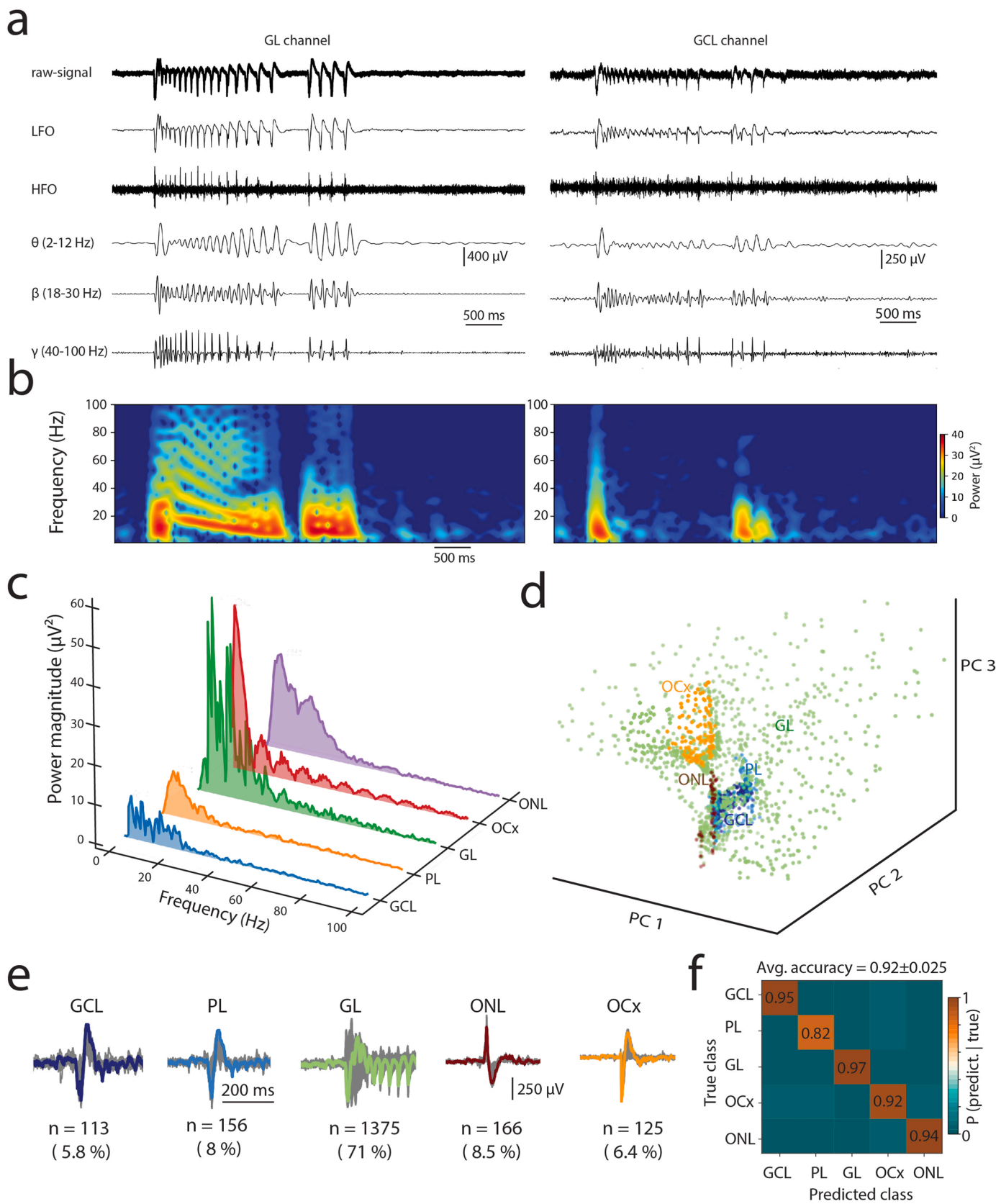
a

GL channel

GCL channel

raw-signal

LFO

HFO

θ (2-12 Hz)

β (18-30 Hz)

γ (40-100 Hz)

400 µV

250 µV

500 ms

500 ms

b

Frequency (Hz)

Power (µV²)

500 ms

c

Power magnitude (µV²)

Frequency (Hz)

ONL
OCx
GL
PL
GCL

d

PC 3

OCx

GL

ONL

PL

GCL

PC 2

PC 1

e

GCL

PL

GL

ONL

OCx

200 ms

250 µV

n = 113
( 5.8 %)

n = 156
( 8 %)

n = 1375
( 71 %)

n = 166
( 8.5 %)

n = 125
( 6.4 %)

f

Avg. accuracy = 0.92±0.025

True class

GCL    0.95
PL         0.82
GL                0.97
OCx              0.92
ONL                    0.94

P (predict. | true)

GCL   PL   GL   OCx   ONL
Predicted class

*(caption on next page)*

**Fig. 3. Network-wide oscillation features and waveforms signatures. a)** Representative event traces from large-scale CMOS-chip recording sites showing low to high ranges of oscillatory frequencies in GL and GCL layers. Exemplary signals from the GL and GCL show wide biosignal signatures of spikes and LFPs with frequency components (θ, β, and γ bands) and high-frequency oscillations (130–300 Hz), indicating multiunit spiking activity. **b)** Pseudo-color spectrograms showing the Frequency-time dynamics in GL and GCL layers. **c)** Representative power spectral density analysis depicts the LFP signals' strength regarding their broadband oscillation in OB layers. It displays a high power magnitude of the θ band in the GL. **d)** Classification of multilayered OB oscillatory waveform shapes profiled with the PCA analysis and K-means algorithm based on features extracted from the LFP events. **e)** Cross-layer classified waveforms (average waveforms are in colors that correspond to the class of OB layer, and grey waveforms showing all extracted extracellular waveforms indicated by *n* and its percentage of the total detected waveforms). **f)** The confusion matrix of k-means clustering-based classification indicating the accuracy of class separation, where true clusters were compared with their predicted ones, indicating a well-defined separation of the OB waveform shapes with an average accuracy of $0.92 \pm 0.025$ computed as the mean of the five diagonal probabilities. (For interpretation of the references to color in this figure legend, the reader is referred to the Web version of this article.)

locked oscillation.

### 3.4. Mapping the spatiotemporal firing patterns for global circuit dynamics

Coherent oscillatory activity in the olfactory circuit is rendered by the spatiotemporal LFP patterns across the OB layers. We sought to exploit BIONICS to quantify the spatial mapping of large-scale firing rate encoded in the whole OB interconnected layers. To do so, we computed the spatial coherence as the correlation of the encoded firing rates of interelectrode distance. The spatial extent of LFP rates is derived from each pixel in the 4096-microelectrode array to capture the dynamics of rhythmic components in space and estimate the breadth of activity origin. Thus, higher coherent electrodes have more regulated LFP firing in a specific cluster of the OB region in space, while lower coherent electrodes show more nonstationary and lower firing activity. In all recorded OB slices, coherence increased across evoked-activity conditions (spontaneous vs. 4AP, BiC, and MK-801, respectively) due to increased spatial rate coding under the activation of more cells in the OB circuits (Fig. 4a). We also computed and quantified the population average of the spatial coherence across the pharmacological conditions divided over bins by groups (Fig. 4b and inset). Despite analogous peaks in all groups, the spontaneous and 4-AP groups do not extend the right tail, as in the BiC and MK-801 groups, indicating recorded electrodes with low coherence values. On the other hand, the distributions of BiC and MK-801 groups are shifted to the right, showing an increase in spatial coherence for the average oscillatory activity in the whole OB neuronal circuit. These significant changes in the spatial coherence may set new standard values, especially in the GL layer (i.e., greater than 0.3), which meet the criteria for considering the GL as a morpho-functional basis of the spatial coding in the early processing of the sensory input (Lledo and Lagier, 2006).

The OB actively creates a spatiotemporal coding space to process complex representations; and simultaneously requires continuous optimization in their distributions, while all these communications are mechanistically coordinated by neural coherence (Fries, 2005). In light of this, we tested the spectral coherence level of oscillatory LFPs and their occurring frequency in all OB interconnected layers under pharmacological conditions. By computing the pairwise coherence spectra between all firing electrodes in all OB layers, we identified a significant increase in the coherence of all oscillatory rhythms (theta, beta, and gamma) but more prominently in the theta rhythms (i.e., encoding significant spatiotemporal information) in all layers under MK-801 compared to BiC (Supplementary Fig. 3). We also found that the coherence at beta oscillations significantly increased in layers connected to OCx (i.e., GL-OCx, PL-OCx, and GCL-OCx) under MK-801 over BiC treatment. These findings support the notion that our recordings preserved rhythmic theta and gamma oscillations in all cross-OB layers and a salient elevation of beta rhythms of firing electrodes in layers

projecting to OCx with NMDA-receptor-dependent modulation. In turn, this may enhance circuit dynamics through a large coding space for optimizing the spatiotemporal representation s (Laurent, 2002). On the whole, based on the communication through coherence concept that selective communication among neuronal ensembles is achieved by the frequency of coherent firing rate oscillations in two spatially connected regions, our results illustrated cross-frequency synchrony in the OB space with prominently increased theta oscillations for encoding information that was mediated by the NMDA-receptor activation. To our knowledge, no previous biosensing platforms have reported microscopic spatial and temporal coherent oscillatory synchronization from the cross-OB layers in the same slice, primarily due to the lack of resolution and insufficient SNR of recorded signals. It is noteworthy that information is encoded in the OB neural architecture by population coding; hence it is essential to record from the entire bulbar network to measure the coherent oscillations of cell assemblies to reveal the mechanistic consequence underlying spatiotemporal coding and decoding. Thus, pharmacological-evoked responses were only studied with smaller-scale electrophysiological and label-based readouts (TIAN et al., 2017; Zhuang et al., 2021; Micholt et al., 2013; Spors et al., 2006), which overshadowed the simultaneous interactions in the entire OB network and its connection to downstream subcortical and cortical areas. However, a further integrative investigation is needed to identify the differential role of these coherent oscillatory interactions/synchronization and their cellular mechanisms underlying computational organization.

### 3.5. Localized initiation and large-scale propagation of synchronized oscillatory activity

In a multilayered OB circuit, the site of generation and spatial propagation of rhythmic electrical patterns are critical for the integrative activity of olfactory information processing. We used the simultaneous recordings from all OB layers to compute the initiation of the field potential signals and trace the spatiotemporal propagation of individual synchronized events. Fig. 4c, Supplementary Fig. 4, and Supplementary Movie 2 show multi-frame pseudo-color images of the LFP oscillatory activity overlaid on the OB circuit's corresponding anatomical regions. In the case of MK-801 treatment, the input signal is processed at the ONL. The oscillatory activity is initiated in the GL layer, propagates across GCL and PL layers to finally send output at the OCx layers. These characterized patterns sculpt complex propagation dynamics of the cellular mechanisms underlying the spatiotemporal coordination of information processing displayed by glomerular, mitral, and granule cells in the OB circuit.

Furthermore, Fig. 4d shows the horizontal propagation of the LFPs across all OB layers. The dynamical propagation is illustrated as the time shift of the peak of the oscillatory events of exemplified signal traces selected from five electrodes located in different OB layers.

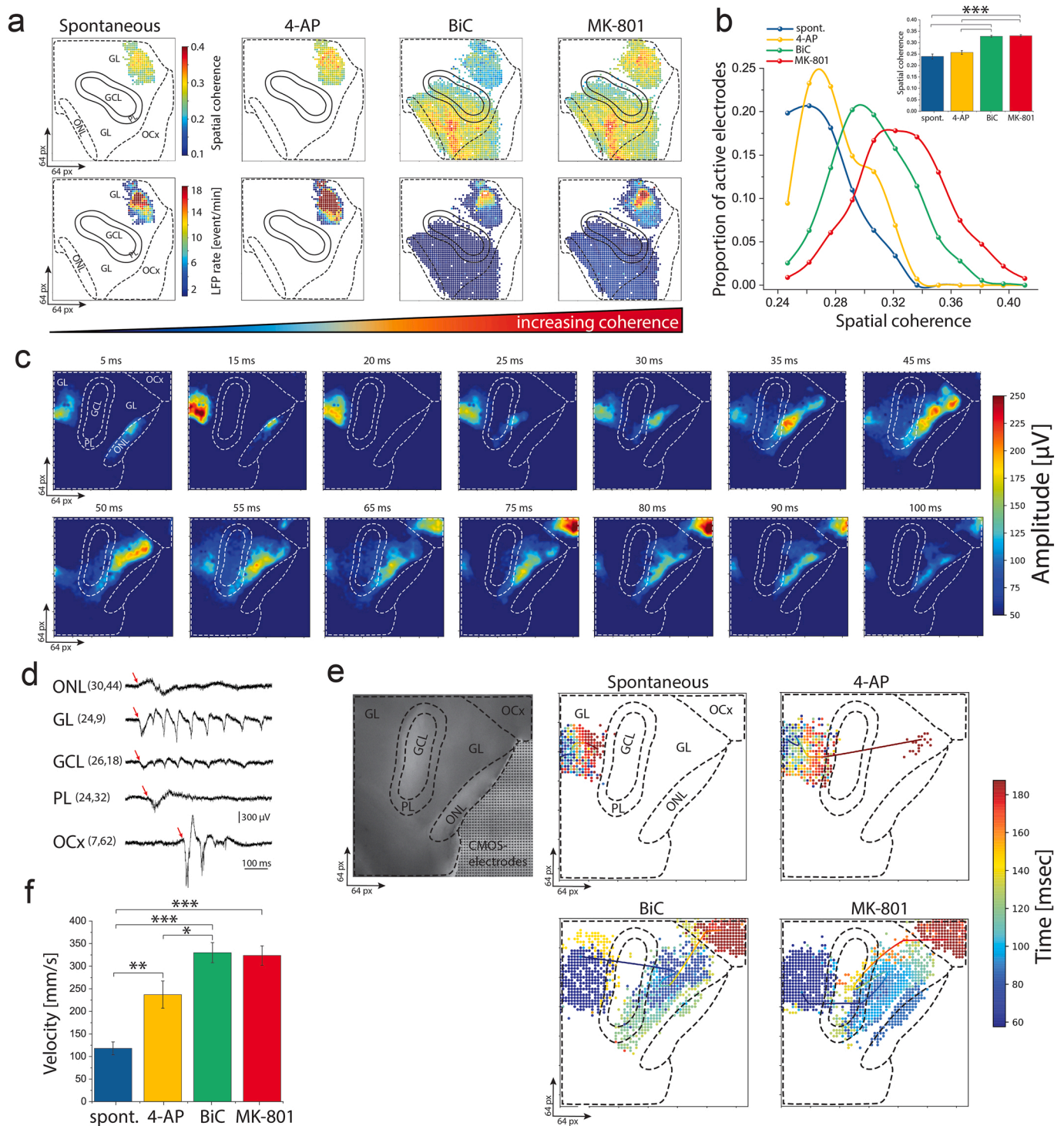Next, to quantitatively investigate the propagation dynamics in

**Fig. 4. Topographical analysis of spatiotemporal dynamics of coding information. a)** Spatial coherence maps displaying correlated pairs of recorded sites in the OB circuit. Maps on top showing the coherence, and at the bottom are the maps of firing information encoded in field potentials. Spatial coherence increasing sequentially by pharmacological treatment of 4-AP, BiC, and MK-801, respectively, yielding more active electrodes encoding higher information of the firing rate of that spectral frequency component (i.e., in the GL). **b)** Spatial coherence quantification showing a significantly shifted distribution towards higher coherence values under drug-treatment compared with spontaneous activity and summarized in (b, inset) (***$p < 0.001$, ANOVA, $n = 24$ slices from 8 mice). **c)** Profile of propagation sequence of representative LFP event showing a defined initiation (ONL and GL) and dynamic propagation of the LFP firing patterns in the OB interconnected circuitry (sending output at the OCx). **d)** Temporal event traces corresponding to active recording sites in different OB layers. The red arrows point to the initiation time and shift to the right to indicate the propagation sequence (i.e., initiated in ONL-GL and terminates at OCx). **e)** Averaged CATs superimposed to the propagating active electrodes and the morphological structure of the OB layers. Time color-coded scale (*right*) indicates the CATs propagation profile and the firing electrodes of a single LFP event. **f)** Velocity of conduction of propagating LFP events is significantly increased when recording performed with 4-AP, BiC, and MK-801 compared to spontaneous (*$p < 0.05$, **$p < 0.01$, ***$p < 0.001$ ANOVA, $n = 24$ slices from 8 mice). (For interpretation of the references to color in this figure legend, the reader is referred to the Web version of this article.)
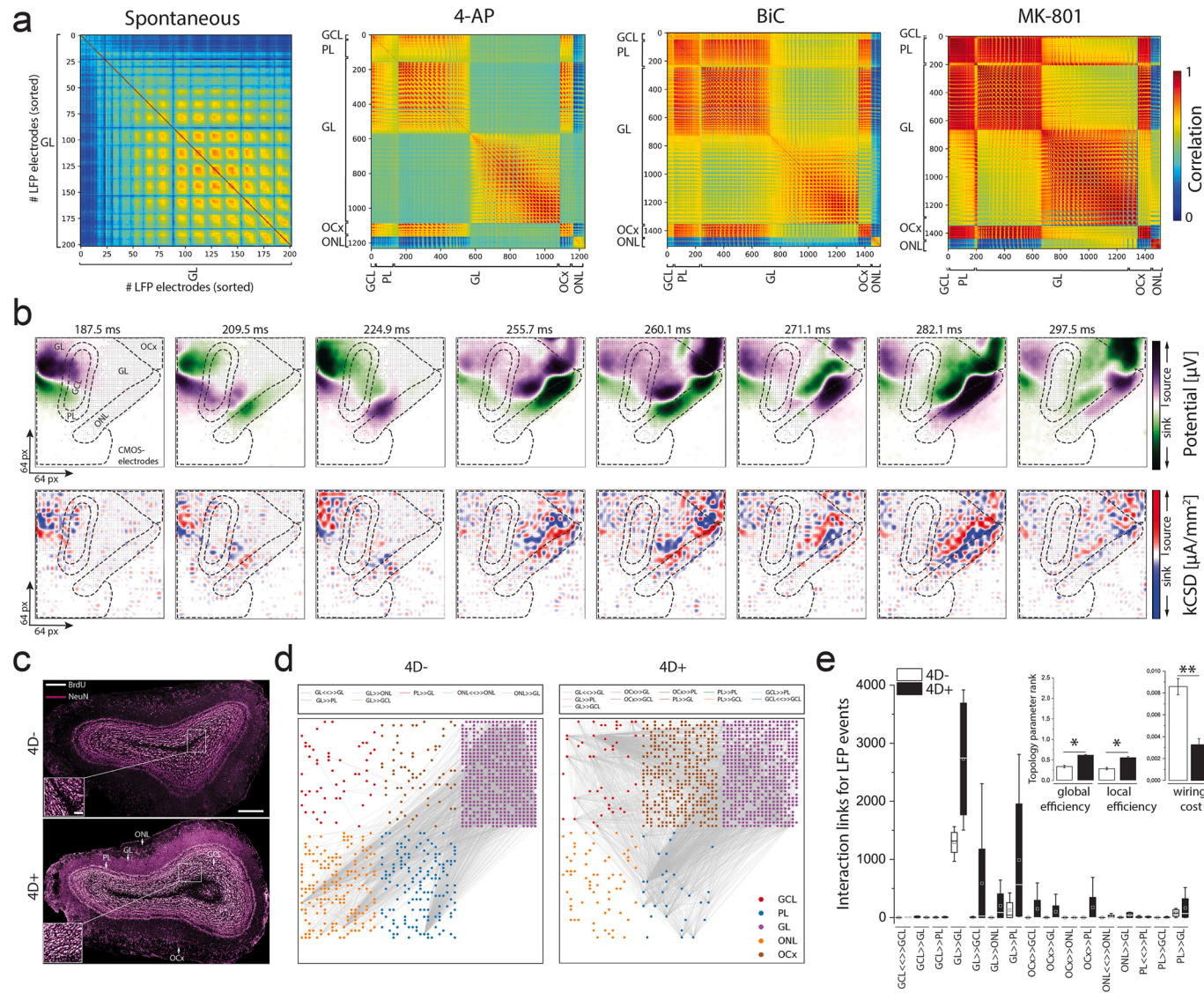
**Fig. 5. Large-scale functional connectivity analysis and validation on dynamical circuit remodeling. a)** Functional connectivity matrices of different active regions of the OB circuit computed using the cross-correlation method for each pair of active electrodes in the 4096-array. In the spontaneous phase, only electrodes of the GL layer showed correlation to each other. The cross-correlation matrices in 4-AP, BiC, and MK-801 treatment indicate higher connectivity with more electrodes simultaneously fired and higher network synchronization than spontaneous recordings. **b)** The temporal evolution of a 2D kCSD construction (bottom) from the LFP recordings (top) for ongoing 100 ms activity. The kCSD indicates the sources (red tones) and sinks (blue tones) during the global field potential activation of the entire OB circuit. **c)** Evident OB neurogenesis effect in 4D+ mouse model as obtained from (Bragado Alonso et al., 2019). Confocal micrographs showing 4D+ slices with higher expression of NeuN+/BrdU+ of newborn integrated neurons mainly in the GCL compared to 4D-. Scale bars represent 500 μm (whole OB) and 100 μm insets. **d)** Direction-based functional connections of interactive pairs of firing electrodes in 4D- and 4D+ recordings computed using Granger causality and DTF algorithms. Grey links showing only 20% of the total detected links on 64x64 CMOS-recording array and are sorted in 6 clusters of the OB layers. **e)** Quantification of (D) showing significantly higher unidirectional and bidirectional interactive links in the 4D+ compared to 4D- (*$p < 0.05$, ANOVA). (E, inset) showing the effect of induced OB neurogenesis on the topological network parameters of efficiency (*$p < 0.05$, ANOVA) and cost of information processing in the entire OB circuit (**$p < 0.01$, ANOVA, $n = 12$ slices from 4 mice). 4D+ indicates higher network efficiency at a lower wiring cost compared to 4D- group. (For interpretation of the references to color in this figure legend, the reader is referred to the Web version of this article.)

detail and identify the ignition site of the location-weighted average of spatiotemporal LFP patterns, we employed a population parameter using the center-of-activity trajectories (CAT) (Chao et al., 2007). We calculated the CAT mean for each electrode by integrating the total number of LFP events in 200 ms voltage-coded movies (see methods). We performed the CAT analysis on the spontaneous, 4-AP, BiC, and MK-801 groups that showed distinct ignition sites in the GL layer in all groups, with a dynamic population propagation towards the OCx in BiC and MK-801 (Fig. 4e).

Furthermore, measuring a multi-site relation of spatiotemporal differences of occurring events allowed us to compute the instantaneous velocity of displacements of the CATs of LFP events in spontaneous and pharmacologically-induced groups to describe the dynamic of spreading activity within the interconnected layers of the OB circuitry. We found a range of propagation mean velocities of CATs ranged from ($117 \pm 17$ to $323.67 \pm 21.4$ mm/s) in spontaneous and MK-801 groups, respectively (Fig. 4f). These values are in the range of previously reported olfactory bulb velocity of conduction in rats (250–460 mm/s) (Keller et al., 1998; Senseman, 1996).

In sum, these results display the global dynamics of the OB population activity by incorporating the physical location of the electrode and the neuronal firing patterns of the multilayered OB circuitry. Also, illustrate evidence of spatial changes in interconnected neuronal populations of the bulbar rhythmogenesis upon blocking the dendrodendritic synaptic connections with MK-801. Similar results were also confirmed by previous in vivo reports on the role of NMDA receptor blockade for dendrodendritic inhibition concluded in smaller-scale electrophysiological and molecular readouts (Schoppa, 1998; Didier et al., 2001).

### 3.6. Multilayered OB functional decomposition for network-wide connectivity

The intricate spatiotemporal propagation patterns illustrated in the previous section involve diverse local neuronal connectivity necessary to synchronize the OB population. To unravel OB circuitry's complexity to understand the underlying information processing, we have examined the emergence of inter-bulbar functional connectivity patterns as a network of pairwise firing electrode interactions. In this context, we computed the Pearson correlation between all LFP firing electrode pairs and performed the OB regional clustering to identify the level of synchronization (Fig. 5a). Quantitatively, the cross-correlation increased significantly after pharmacological treatment with 4-AP, BiC, and MK-801 compared to the baseline spontaneous activity (Supplementary Fig. 5). Further, by tracing the emergence of functional links from spontaneous to MK-801-evoked activity, we found in the GL, predominant distinct populations of activated ensembles forming hub microcircuits and connecting OB subregions circuitry (Supplementary Fig. 6). This mesoscale rewiring of those new connections is signaled by the activity-dependent changes processed by the contemporary firing ensembles in the GL and determined the interareal coordination and reorganization of the population activity. These results illustrate individual neuronal ensembles' contribution to the OB network synchrony in ever-available detail. Further, help to identify the critical OB subregions for optimizing network patterns in a large-scale spatial organization.

### 3.7. Identifying OB neuronal transmembrane current source and sink generators

Next, we further exploited our platform to pinpoint the high spatiotemporal resolution of local field generators (i.e., sources and sinks) in the inter-bulbar circuitry as emerged from the oscillatory activity of OB neuronal ensembles. Thus, we constructed bidimensional maps employing the kCSD method (Potworowski et al., 2012) to estimate the average transmembrane currents extracted from the field activity recordings (Fig. 5b, and Supplementary Movie 3). At the beginning of the LFP activation ($t = 187.5$ ms), the KCSD maps (Fig. 5b, *bottom*) showed defined topographic activation features indicated by stronger and focused source generators (red color-coded in the GL and GCL layers with defined cellular identity (i.e., the microelectrodes underlying the transmembrane dipole). In contrast, the potential maps (Fig. 5b, *top*) showed general activation with no topographical differences in the GL and GCL layers. The computed propagating source-sink generators accompanied the oscillatory synchronized activation dynamically across OB layers. These current generators are eventually conveyed information at the OCx layers ($t = 297$ ms) but provided more defined and sharper localization of the cellular neuronal activation (i.e., in the OCx, multiple sources revealed by kCSD while only sinks were detected in the potential maps). These results demonstrate remarkable advantages in defining and mapping disjoint sets of sinks and sources of the OB oscillatory activity compared to potential measures in terms of strength of neuroelectrical activation and spatial topographic patterns. This allows us to circumvent field potentials' ambiguity and pinpoint the LFP generators at a high spatiotemporal resolution to capture with fidelity the correlated functional and individual cellular elements.

### 3.8. Large-scale recordings validating enhanced OB-wide network connectivity and efficiency with adult neurogenesis

Next, to validate the significance of our large-scale recordings, we sought to examine the impact of ongoing neurogenesis on the dynamic of cross-scale OB circuitry and olfaction improvement. Thus, we used a genetically modified mouse model allowing the inducible expansion of neural stem cells by overexpression of Cdk4/cyclinD1 (4D+) in neural stem cells and using littermate (4D-) mice as negative controls (Bragado Alonso et al., 2019). Structurally, the 4D+ group has shown a neuronal expansion and increased neurogenesis indicated by the NeuN+/BrdU + staining compared to the 4D- group (Fig. 5c) (Bragado Alonso et al., 2019). On the other hand, standard patch-clamp whole-cell recordings reported no significant functional and electrophysiological differences between 4D+ and 4D- group (Bragado Alonso et al., 2019). Thus, here, we obtained OB-wide patterns of activity from 4D+ and 4D- groups. Then, we applied the Granger causality as a connectivity method (Brovelli et al., 2004; Granger, 1969) to quantify the directional information flow in the OB layers rendered by all pairwise electrode interactions (Fig. 5d). The 4D+ group showed significantly higher unidirectional (GL→ GCL, OCx →GL, GCL, PL) and bidirectional (GL→GL, PL, ONL) interactions compared with the 4D- group (Fig. 5e).

However, despite the localized functional induction by the new neurons in the GCL layer of the 4D+ group, the neurogenic effect significantly enhanced the global performance capacity of information processing in the entire interconnected OB circuitry, thus promoting network economy (Achard and Bullmore, 2007). To this highlight, our results demonstrate the trade-off between network cost and efficiency indicated by the increased interconnection density between OB layers, reduced physical cost (i.e., wiring cost), and increased local and global efficiencies of information transfer of the spatially connected neuronal ensembles (Fig. 5e inset) (see methods). Remarkably, our results also conclud network-wide functional remodeling properties that were unfeasible in smaller-scale electrophysiological methods.

## 4. Conclusions and outlook

The unmet need for large-scale multi-site biosensing techniques limits the understanding of information processing in the olfactory system. It also hampers implementing biomimetic olfactory-based biosensors to exploit olfaction in fundamental applications. Dense microchips composed of thousands of electrodes could overcome this limitation and reveal the olfactory spatiotemporal dynamics. Thus, we have devised BIONICS (Biohybrid Olfactory Neural Circuit on a CMOS-chip), a novel platform with high-density CMOS-based active circuit architecture for simultaneously recording from thousands of OB neuronal ensembles to delineate large-scale spatiotemporal morphofunctional plasticity in the multilayered OB circuitry.

These recordings are facilitated by functionalizing the CMOS-chip surface with the adhesion-promoting molecule (PDLO). This allowed a homogenous and effective electrical coupling of the neuro-electrode-wide interface (i.e., generation of a high seal resistance) that fostered cellular activity stability and optimal SNR. Accelerating development in bioelectronics nose platforms hinges on the measurement technique and biosensing instruments as well as complex analytical tools for acquiring fundamental insights about the recorded biosignals. Thus, we employed rigorous algorithms and statistical analysis to catalyze significant parameters and insights from our multidimensional recorded data.

We have attributed the inhomogeneity and sparsity of OB cross-scale functional representations to their skewed lognormal LFP distributions driven by a balance between excitatory and inhibitory neuronal populations to provide network stability and reliable information processing for spatiotemporal coding.

We further characterized the firing patterns and their dynamical features across the OB-wide network by classifying the waveform shapes based on their rich inherent information in their nonsinusoidal oscillations. These results can inspire computational models and analytical methods to correlate these distinct waveforms to their underlying biophysical generators to describe disease conditions or behavioral states.

Also, facilitated by multi-site measurements of pharmacological-induced activity, we concluded the emergence of spatiotemporal network coherence, initiation of the LFP oscillations, and their cross-scale propagational dynamics at high spatiotemporal resolution.

The large number of recording sites in the CMOS-array confer sufficient access to simultaneous neuronal ensembles, enabling the construction of high-resolution 2D network-wide functional connectivity matrices and kCSD maps of local field potentials. Thus, providing a plausible method to probe the intrinsically sparse OB network connectivity and the contribution of local microcircuits and inhomogeneities in the LFP generation.

Our study suggests a new tool to address plasticity underlying olfactory spatiotemporal coding, not accessible with current imaging and electrophysiological techniques. Remarkably, we have specifically assessed the large-scale functional remodeling in the OB circuit that involved integrating newly generated neurons in the GCL layer of a mouse model with enhanced neurogenesis. We elucidated the induced functional neurogenic effect for enhancing OB network performance by integrating wide-effective information rendered by the topological organization and the local and global network efficiency. This would suggest a new generation of biologically inspired smart dynamical biomimetic systems and computational models capable of achieving faster and optimized olfactory information processing and enabling optimal selectivity and sensitivity for challenging applications. It is noteworthy that the advancement of chemosensory biosensors hinges on the large hyperspace of multidimensional biochemical features and the procedures for extraction and optimization toward application-specific goals (Göpel, 1998, 2000). In light of this and besides the contribution to investigate the spatiotemporal coding in the OB circuitry, our platform can provide substantial support to future development in neuromorphic olfaction and biomimetic olfactory-based biosensors derived from: i) CMOS-based architecture that offers miniature, low-power, low-cost design to implement various olfactory-based biosensors; ii) large-scale circuit-level organization, spatiotemporal encoding information, optimized tissue-electrode interface, and low noise detection rendering considerable benchmarks for improving the shortcomings of current olfactory biosensors for signal processing and pattern computations; iii) olfactory bulb computational principles extracted from our biological data can inspire designing radically different neuromorphic algorithms and implementing novel hardware; iv) a platform that is equally applicable to other olfactory systems and species (i.e., epithelium and olfactory receptor neurons) to map the multi-odor-evoked responses.

In sum, our work has attempted to paint with a large-scale neurotechnological approach the breath and wonders of the chemosensory olfaction system. BIONICS has meticulously broken down the intricate firing patterns associated with olfactory code, promising progress not only toward understanding neural processing of sensory information in the olfactory system but the biomimetic design of a bioelectronic nose and artificial chemosensory system development that may provide specific biomarkers for health and disease.

## CRediT authorship contribution statement

**Xin Hu:** Wrote the code for analysis and analyzed the data. **Shah-rukh Khanzada:** Performed part of experiments and analyzed the data. **Diana Klütsch:** Performed OB slicing and technical support. **Federico Calegari:** Provided the mouse line and data concerning the 4D overexpression system. **Hayder Amin:** Project conceptualization, planning, and management, designed & performed experiments, analyzed the data and wrote the manuscript. All authors revised, reviewed, and approved the final version of the manuscript.

## Declaration of competing interest

The authors declare that they have no known competing financial interests or personal relationships that could have appeared to influence the work reported in this paper.

## Acknowledgment

## Appendix A. Supplementary data

Supplementary data to this article can be found online at https://doi.org/10.1016/j.bios.2021.113834.

## References

Achard, S., Bullmore, E., 2007. Efficiency and cost of economical brain functional networks. PLoS Comput. Biol. 3, 0174–0183.

Alfinito, E., Pennetta, C., Reggiani, L., 2010. Olfactory receptor-based smell nanobiosensors: an overview of theoretical and experimental results. Sensor. Actuator. B Chem. 146, 554–558.

Amin, H., et al., 2016. Electrical responses and spontaneous activity of human iPS-derived neuronal networks characterized for 3-month culture with 4096-electrode arrays. Front. Neurosci. 10, 1–15.

Amin, H., Nieus, T., Lonardoni, D., Maccione, A., Berdondini, L., 2017a. High-resolution bioelectrical imaging of Aβ-induced network dysfunction on CMOS-MEAs for neurotoxicity and rescue studies. Sci. Rep. 7, 2460.

Amin, H., Marinaro, F., Tonelli, D.D.P., Berdondini, L., 2017b. Developmental excitatory-to-inhibitory GABA-polarity switch is disrupted in 22q11.2 deletion syndrome: a potential target for clinical therapeutics. Sci. Rep. 7, 1–18.

Amin, H., Dipalo, M., De Angelis, F., Berdondini, L., 2018. Biofunctionalized 3D nanopillar arrays fostering cell-guidance and promoting synapse stability and neuronal activity in networks. ACS Appl. Mater. Interfaces 1–9. https://doi.org/10.1021/acsami.8b00387.

Angotzi, G.N., et al., 2019. SiNAPS: an implantable active pixel sensor CMOS-probe for simultaneous large-scale neural recordings. Biosens. Bioelectron. 126, 355–364.

Artegiani, B., Lindemann, D., Calegari, F., 2011. Overexpression of cdk4 and cyclinD1 triggers greater expansion of neural stem cells in the adult mouse brain. J. Exp. Med. 208, 937–948.

Berdondini, L., et al., 2005. High-density electrode array for imaging in vitro electrophysiological activity. Biosens. Bioelectron. 21, 167–174.

Berdugo-Vega, G., et al., 2020. Increasing neurogenesis refines hippocampal activity rejuvenating navigational learning strategies and contextual memory throughout life. Nat. Commun. 11.

Bragado Alonso, S., et al., 2019. An increase in neural stem cells and olfactory bulb adult neurogenesis improves discrimination of highly similar odorants. EMBO J. 38, e98791.

Brovelli, A., et al., 2004. Beta oscillations in a large-scale sensorimotor cortical network: directional influences revealed by Granger causality. Proc. Natl. Acad. Sci. U. S. A 101, 9849–9854.

Buck, L., Axel, R., 1991. A novel multigene family may encode odorant receptors: a molecular basis for odor recognition. Cell 65, 175–187.

Bushdid, C., Magnasco, M.O., Vosshall, L.B., Keller, A., 2014. Humans can discriminate more than 1 trillion olfactory stimuli. Science (80) 343, 1370–1372.

Buzsáki, G., 2004. Large-scale recording of neuronal ensembles. Nat. Neurosci. 7, 446–451.

Buzsáki, G., Draguhn, A., 2004. Neuronal olscillations in cortical networks. Science 304, 1926–1929.

Buzsáki, G., Anastassiou, C.A., Koch, C., 2012. The origin of extracellular fields and currents-EEG, ECoG, LFP and spikes. Nat. Rev. Neurosci. 13, 407–420.

Chao, Z.C., Bakkum, D.J., Potter, S.M., 2007. Region-specific network plasticity in simulated and living cortical networks: comparison of the center of activity trajectory (CAT) with other statistics. J. Neural. Eng. 4, 294–308.

Cooper Roddey, J., Girish, B., Miller, J.P., 2000. Assessing the performance of neural encoding models in the presence of noise. J. Comput. Neurosci. 8, 95–112.

Damos, P., 2016. Using multivariate cross correlations, Granger causality and graphical models to quantify spatiotemporal synchronization and causality between pest populations. BMC Ecol. 16.

Diclehan, A., Oguzhan, U., Mehmet, T., 2019. Electronic Nose and Its Applications: A Survey. Int. J. Autom. Comput. doi:10.1007/s11633-019-1212-9..

Didier, A., et al., 2001. A dendrodendritic reciprocal synapse provides a recurrent excitatory connection in the olfactory bulb. Proc. Natl. Acad. Sci. U. S. A 98, 6441–6446.

Ding, C., He, X., 2004. Cluster structure of K-means clustering via principal component analysis. In: Lecture Notes in Computer Science (Including Subseries Lecture Notes in Artificial Intelligence and Lecture Notes in Bioinformatics), vol. 3056. Springer Verlag, pp. 414–418.

Doucette, W., et al., 2011. Associative cortex features in the first olfactory brain relay station. Neuron 69, 1176–1187.

Dung, T.T., et al., 2018. Applications and advances in bioelectronic noses for odour sensing. Sensors (Switzerland) 18.

Eggermont, J.J., Munguia, R., Pienkowski, M., Shaw, G., 2011. Comparison of LFP-based and spike-based spectro-temporal receptive fields and cross-correlation in cat primary auditory cortex. PLoS One 6.

Fries, P., 2005. A mechanism for cognitive dynamics: neuronal communication through neuronal coherence. Trends Cognit. Sci. 9, 474–480.

Fukunaga, I., Herb, J.T., Kollo, M., Boyden, E.S., Schaefer, A.T., 2014. Independent control of gamma and theta activity by distinct interneuron networks in the olfactory bulb. Nat. Neurosci. 17, 1208–1216.

Gandolfo, M., Maccione, a, Tedesco, M., Martinoia, S., Berdondini, L., 2010. Tracking burst patterns in hippocampal cultures with high-density CMOS-MEAs. J. Neural. Eng. 7, 056001.

Gelperin, A., Tank, D.W., 1990. Odour-modulated collective network oscillations of olfactory interneurons in a terrestrial mollusc. Nature 345, 437–440.

Gelperin, A., Rhines, L.D., Flores, J., Tank, D.W., 1993. Coherent network oscillations by olfactory interneurons: modulation by endogenous amines. J. Neurophysiol. 69, 1930–1939.

Göpel, W., 1998. Chemical imaging: I. Concepts and visions for electronic and bioelectronic noses. Sensor. Actuator. B Chem. 52, 125–142.

Göpel, W., 2000. From electronic to bioelectronic olfaction, or: from artificial 'moses' to real noses. Sensor. Actuator. B Chem. 65, 70–72.

Granger, C.W.J., 1969. Investigating causal relations by econometric models and cross-spectral methods. Econometrica 37, 424.

Holt, G.R., Softky, W.R., Koch, C., Douglas, R.J., 1996. Comparison of discharge variability in vitro and in vivo in cat visual cortex neurons. J. Neurophysiol. 75, 1806–1814.

Hurley, N., Rickard, S., 2009. Comparing measures of sparsity. IEEE Trans. Inf. Theor. 55, 4723–4741.

Ikegami, A., Kaneyasu, M., 1985. Olfactory detection using integrated sensors. In: *Olfactory Detection Using Integrated Sensors* 136–139 (Proc. 3rd Int. Conf. Solid-State Sensors and Actuators (Transducers'85), Philadelphia, PA, USA (7111985).

Imai, T., 2014. Construction of functional neuronal circuitry in the olfactory bulb. Semin. Cell Dev. Biol. 35, 180–188.

Imam, N., Cleland, T.A., 2019. Rapid online learning and robust recall in a neuromorphic olfactory circuit. Nat. Mach. Intell. 2, 181–191.

Imfeld, K., et al., 2008. Large-scale, high-resolution data acquisition system for extracellular recording of electrophysiological activity. IEEE Trans. Biomed. Eng. 55, 2064–2073.

Ingebrandt, S., 2015. Bioelectronics: sensing beyond the limit. Nat. Nanotechnol. 10, 734–735.

Kaminski, M.J., Blinowska, K.J., 1991. A new method of the description of the information flow in the brain structures. Biol. Cybern. 65, 203–210.

Kay, L.M., 2005. Theta oscillations and sensorimotor performance. Proc. Natl. Acad. Sci. U. S. A 102, 3863–3868.

Kay, L.M., 2014. Circuit oscillations in odor perception and memory. In: Progress in Brain Research, vol. 208. Elsevier B.V.

Keller, A., et al., 1998. Functional organization of rat olfactory bulb glomeruli revealed by optical imaging. J. Neurosci. 18, 2602–2612.

Ko, H.J., Park, T.H., 2005. Piezoelectric olfactory biosensor: ligand specificity and dose-dependence of an olfactory receptor expressed in a heterologous cell system. Biosens. Bioelectron. 20, 1327–1332.

Kwon, O.S., et al., 2015. An ultrasensitive, selective, multiplexed superbioelectronic nose that mimics the human sense of smell. Nano Lett. 15, 6559–6567.

Latora, V., Marchiori, M., 2001. Efficient behavior of small-world networks. Phys. Rev. Lett. 87, 198701-1–198701–4.

Laurent, G., 2002. Olfactory network dynamics and the coding of multidimensional signals. Nat. Rev. Neurosci. 3, 884–895.

Lee, J.Y., Ko, H.J., Lee, S.H., Park, T.H., 2006. Cell-based measurement of odorant molecules using surface plasmon resonance. Enzym. Microb. Technol. 39, 375–380.

Lepousez, G., Valley, M.T., Lledo, P.-M., 2013. The impact of adult neurogenesis on olfactory bulb circuits and computations. Annu. Rev. Physiol. 75, 339–363.

Linster, C., Cleland, T.A., 2001. How spike synchronization among olfactory neurons can contribute to sensory discrimination. J. Comput. Neurosci. 10, 187–193.

Liu, Q., 2015. Olfactory cell-based smell sensors. In: Bioinspired Smell and Taste Sensors, vols. 45–59. Springer Netherlands. https://doi.org/10.1007/978-94-017-7333-1_3.

Liu, Q., et al., 2006. Olfactory cell-based biosensor: a first step towards a neurochip of bioelectronic nose. Biosens. Bioelectron. 22, 318–322.

Lledo, P.M., Lagier, S., 2006. Adjusting neurophysiological computations in the adult olfactory bulb. Semin. Cell Dev. Biol. 17 443–453.

Lledo, P.-M., Gheusi, G., Vincent, J.-D., 2005. Information Processing in the Mammalian Olfactory System. https://doi.org/10.1152/physrev.00008.2004.-Recently.

Margrie, T.W., Schaefer, A.T., 2003. Theta oscillation coupled spike latencies yield computational vigour in a mammalian sensory system. J. Physiol. 546, 363–374.

Micholt, E., et al., 2013. Extracellular recordings from rat olfactory epithelium slices using micro electrode arrays. Sensor. Actuator. B Chem. 184, 40–47.

Mizuseki, K., Buzsáki, G., 2013. Preconfigured, skewed distribution of firing rates in the hippocampus and entorhinal cortex. Cell Rep. 4, 1010–1021.

Mombaerts, P., 2001. How smell develops. Nat. Neurosci. 4 1192–1198.

Mori, K., Nagao, H., Yoshihara, Y., 1999. The olfactory bulb: coding and processing of odor molecule information. Science 286, 711–715 (80-. ).

Panas, D., et al., 2015. Sloppiness in spontaneously active neuronal networks. J. Neurosci. 35, 8480–8492.

Panzeri, S., Ince, R.A.A., Diamond, M.E., Kayser, C., 2014. Reading spike timing without a clock: intrinsic decoding of spike trains. Philos. Trans. R. Soc. B Biol. Sci. 369.

Persaud, K., Dodd, G., 1982. Analysis of discrimination mechanisms in the mammalian olfactory system using a model nose. Nature 299, 352–355.

Petersen, P.C., Berg, R.W., 2016. Lognormal firing rate distribution reveals prominent fluctuation-driven regime in spinal motor networks. Elife 5, 1–33.

Potworowski, J., Jakuczun, W., Łeski, S., Wójcik, D., 2012. Kernel current source density method. Neural Comput. 24, 541–575.

Price, J.L., Powell, T.P., 1970a. The morphology of the granule cells of the olfactory bulb. J. Cell Sci. 7, 91–123.

Price, J.L., Powell, T.P.S., 1970b. The mitral and short axon cells of the olfactory bulb. J. Cell Sci. 7.

Rojas-Líbano, D., Kay, L.M., 2008. Olfactory system gamma oscillations: the physiological dissection of a cognitive neural system. Cogn. Neurodyn. 2, 179–194.

Schaworonkow, N., Nikulin, V.V., 2019. Spatial neuronal synchronization and the waveform of oscillations: implications for EEG and MEG. PLoS Comput. Biol. 15, 1–22.

Schöning, M.J., Schroth, P., Schütz, S., 2000. The use of insect chemoreceptors for the assembly of biosensors based on semiconductor field-effect transistors. Electroanalysis 12, 645–652.

Schoppa, N.E., 1998. Dendrodendritic inhibition in the olfactory bulb is driven by NMDA receptors. J. Neurosci. 18, 6790–6802.

Senseman, D.M., 1996. High-speed optical imaging of afferent flow through rat olfactory bulb slices: voltage-sensitive dye signals reveal periglomerular cell activity. J. Neurosci. 16, 313–324.

Shepherd, G.M., 1972. Synaptic organization of the mammalian olfactory bulb. Physiol. Rev. 52, 864–917.

Spors, H., Wachowiak, M., Cohen, L.B., Friedrich, R.W., 2006. Temporal dynamics and latency patterns of receptor neuron input to the olfactory bulb. J. Neurosci. 26, 1247–1259.

Tian, J., Tu, C., Huang, B., Ye, X., 2017. Extracellular potential recording of patterned rat olfactory bulb neuronal network using planar microelectrode arrays, 3, 69–74.

Wasilewski, T., Gębicki, J., Kamysz, W., 2017. Bioelectronic nose: current status and perspectives. Biosens. Bioelectron. 87, 480–494.

Welch, P.D., 1967. The use of fast fourier Transform for the estimation of power spectra: a method based on time averaging over short, modified Periodograms. IEEE Trans. Audio Electroacoust. 15, 70–73.

Wilkens, W.F., Hartman, J.D., 1964. An electronic analog for the olfactory processes. J. Food Sci. 29, 372–378.

Zhuang, L., et al., 2021. A biohybrid nose for evaluation of odor masking in the peripheral olfactory system. Biosens. Bioelectron. 171, 112737.